Dynamics of Atmospheres and Oceans 69 (2015) 12–25

Contents lists available at ScienceDirect

Dynamics of Atmospheres and Oceans

journal homepage: www.elsevier.com/locate/dynatmoce

Impressions of the turbulence variability in a weakly stratified, flat-bottom deep-sea 'boundary layer'

Hans van Haren *

Royal Netherlands Institute for Sea Research (NIOZ), P.O. Box 59, 1790 AB Den Burg, the Netherlands

ARTICLE INFO

Article history:
Received 15 May 2014
Received in revised form 10 October 2014
Accepted 20 October 2014
Available online 15 November 2014

Keywords:
High-resolution temperature observations
Turbulence in weakly stratified sea
Internal wave shear
Internal-wave-induced slantwise
Convection

ABSTRACT

The character of turbulent overturns in a weakly stratified deep-sea is investigated in some detail using 144 high-resolution temperature sensors at 0.7 m intervals, starting 5 m above the bottom. A 9-day, 1 Hz sampled record from the 912 m depth flat-bottom (<0.5% bottom-slope) mooring site in the central-north Alboran Sea (W-Mediterranean) demonstrates an overall conservative temperature range of only 0.05 °C, a typical mean buoyancy period as large as 3 h and a 1 Hz-profile-vertically-averaged turbulence dissipation rate maximum of only $10^{-8}\,m^2\,s^{-3}$. Nonetheless, this 'boundary layer' varies in height between <6 and >104 m above the bottom and is thus not homogeneous throughout; the temperature variations are seldom quiescent and are generally turbulent in appearance, well exceeding noise levels. The turbulence character is associated with small-scale internal waves; examples are found of both shear- and convection-driven turbulence; particular association, although not phase-locked, is found between turbulence variations and tidal rather than inertial motions; the mean buoyancy frequency of a few times the inertial frequency implies the importance of 'slantwise convection' in the direction of the earth rotational vector over the direction of gravity. Such convection is observed both in near-homogeneous and weakly stratified form.

1. Introduction

As oceans and seas are mainly heated from above, their statically stable vertical density stratification may support considerable internal waves and de-stabilizing vertical current differences 'shear' that may turn into turbulent convection important for the vertical exchange of suspended matter. This shear is predominantly near the inertial frequency f, the lowest internal wave frequency in stratified waters. This is because the vertical length-scale of near-inertial waves is small (LeBlond and Mysak, 1978).

In relatively weak stratification, where the buoyancy frequency N is only a few times f, the convection is no longer in the direction of gravity but tends to the direction of the earth rotational vector $\boldsymbol{\Omega}$, 'slantwise convection' (Straneo et al., 2002; Sheremet, 2004; for a review see Gerkema et al., 2008). Slantwise convection can be set up in a generalized case via vertically sheared currents associated with horizontal density gradients 'fronts' (Marshall and Schott, 1999). In the dynamics governing such convection in near-homogeneous waters, the usually ignored horizontal Coriolis parameter $f_h = 2\,\Omega \cos\varphi$ is

* Tel.: +31 222 369300/369451.
E-mail address: hans.van.haren@nioz.nl (H. van Haren).

http://dx.doi.org/10.1016/j.dynatmoce.2014.10.002
0377-0265/$ – see front matter

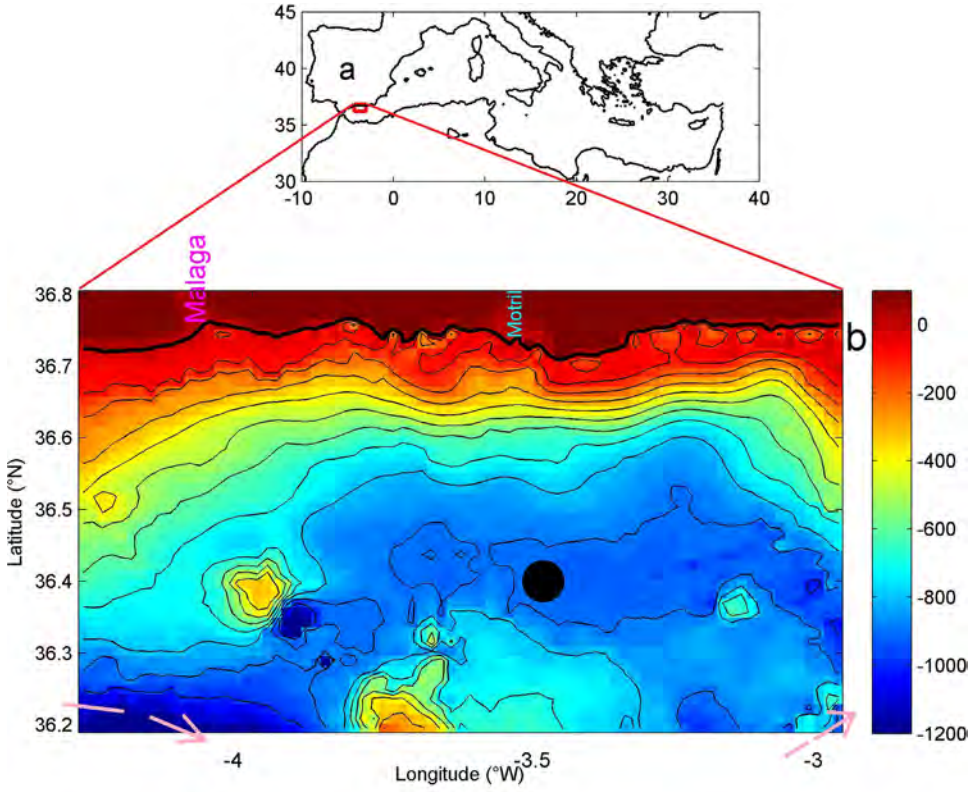

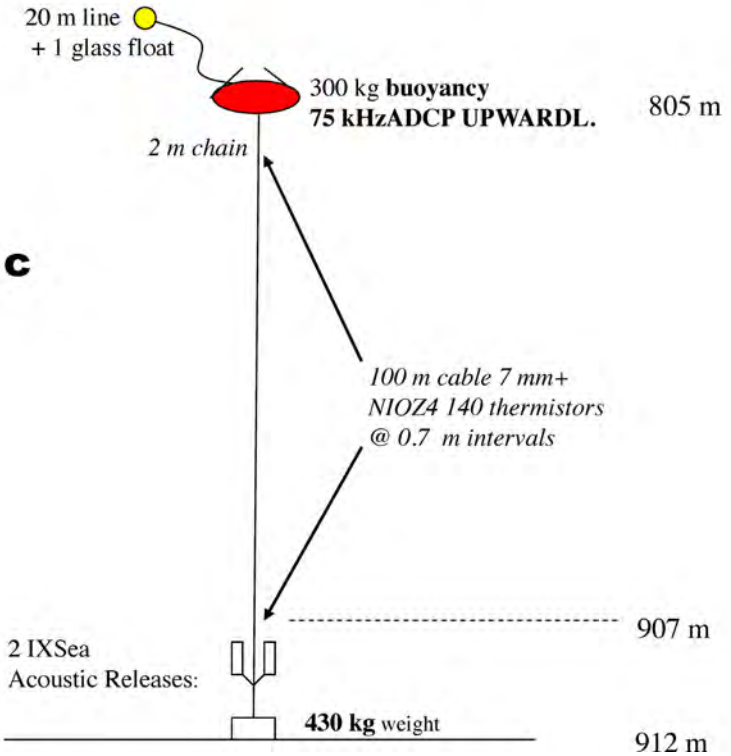

Fig. 1. Mooring information. (a) Mediterranean Sea. (b) Mooring test-site (black dot) in the central-north Alboran Sea Western Mediterranean. The black waterdepth contours are drawn every 500 m; the thick-black contour indicates the 0 m coast-line. The general near-surface Atlantic inflow frontal border is indicated by purple line-arrows (after L'Helguen et al., 2002). (c) Mooring sketch. (For interpretation of the references to color in this figure legend, the reader is referred to the web version of this article.)

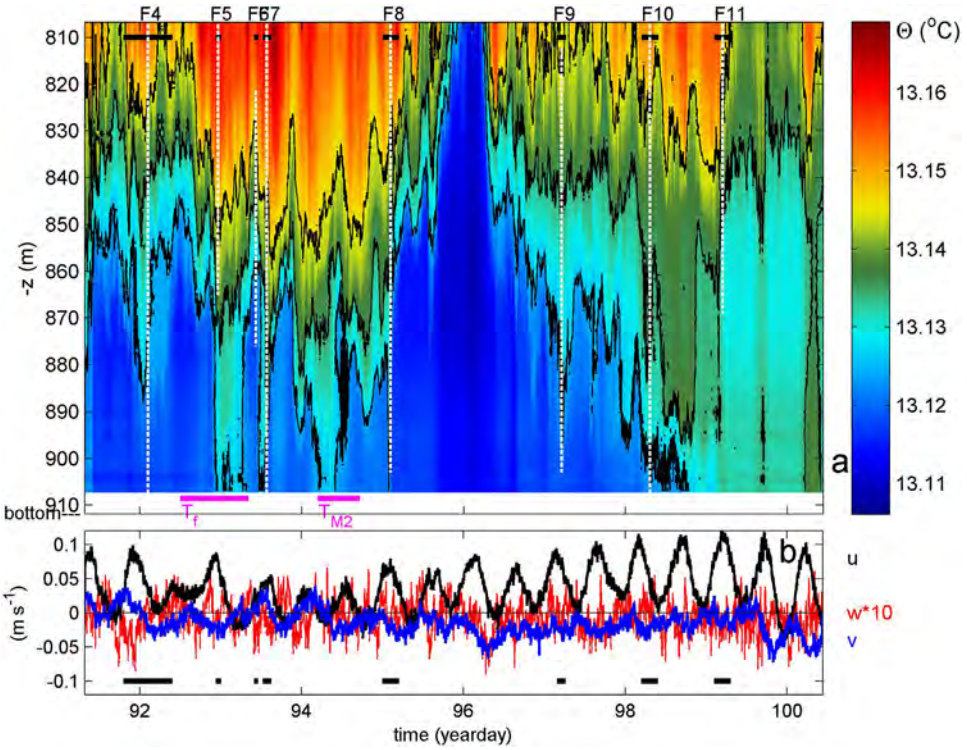

Fig. 2. Overview of 9 days of moored observations from the central-north Alboran Sea in April 2013. (a) Depth–time image of 1 Hz sampled temperature data from 144 sensors moored m intervals between 5 and 105 m above the bottom (mab). Three arbitrary contours are given in black for 13.125, 13.135 and 13.145 °C. The horizontal black bars and vertical white dashed lines indicate short ranges to be displayed in later figures, designated by 'F' followed by their number. The horizontal purple bars indicate the inertial ('f') and semidiurnal lunar tidal ('M_2') periods, for reference. (b) Current components observed at 145 mab in the second lowest depth-interval of a 75 kHz Acoustic Doppler Current Profiler, smoothed over 15 min. Note that the scale of the vertical component is multiplied by a factor of 10. (For interpretation of the references to color in this figure legend, the reader is referred to the web version of this article.)

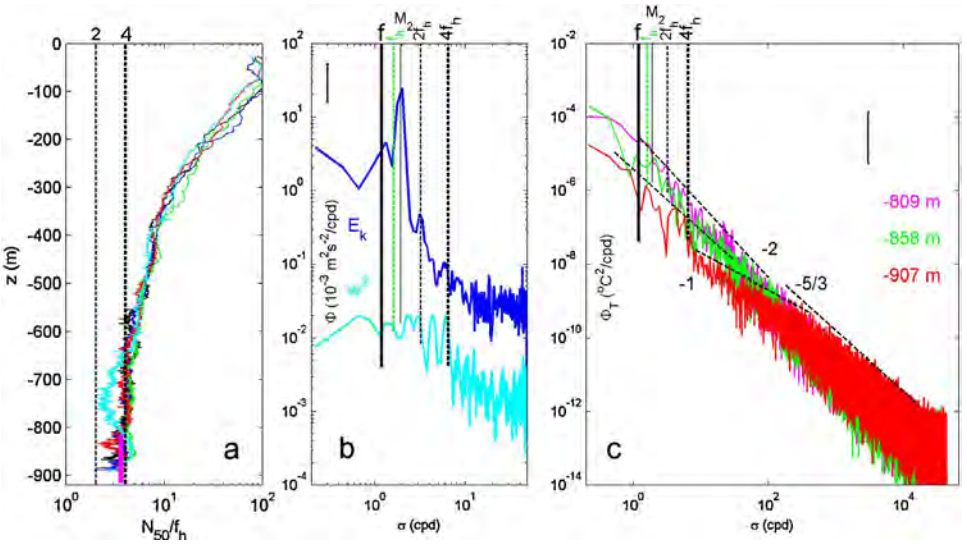

Fig. 3. Stratification and spectral overview. (a) Entire profiles of buoyancy frequency scaled with the local horizontal component of the Coriolis parameter and smoothed over 50 m, from all 5CTD-stations to within 1 km from the mooring. The vertical purple bar near the bottom indicates the range of the moored temperature sensors at their time–(depth) range-mean N/f_h-value. (b) Weakly smoothed (5 degrees of freedom, dof) spectra of current data from Fig. 2b. (c) Weakly smoothed (5 dof) spectra of 1 Hz temperature data from 3 depths in Fig. 2a. For reference, several slopes with frequency are indicated. (For interpretation of the references to color in this figure legend, the reader is referred to the web version of this article.)

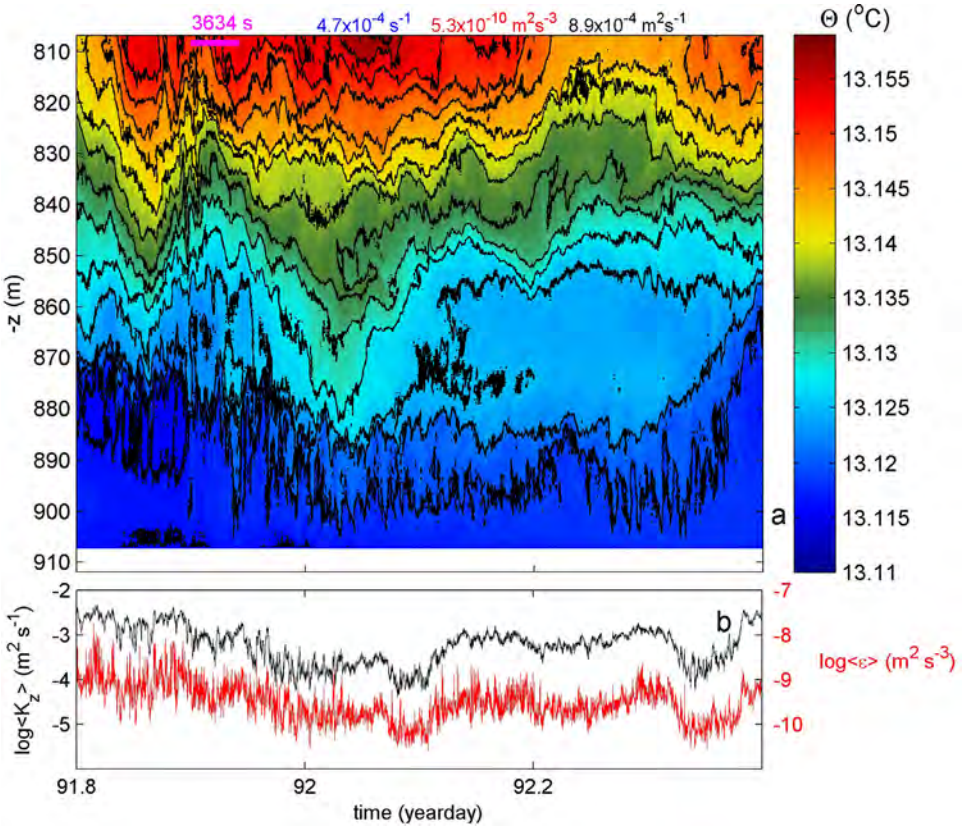

Fig. 4. Approximately half a day (14 h) sample detail of observations showing rapid near-bottom overturns. (a) Conservative temperature over the range indicated by the white-dashed line in Fig. 2a. The black contour lines are drawn every 0.004 °C. At the top, a time reference is given by the purple bar, indicating the shortest buoyancy period found in this data-detail. Values for time-range-mean parameters are given of buoyancy frequency (blue), turbulence dissipation rate (red) and turbulent eddy diffusivity (black). Errors are to within a factor of 2, approximately. (b) Time series of range-mean turbulence parameters estimated from the data in (a). using the method of reordering overturns (Thorpe, 1977; cf. Appendix A). (For interpretation of the references to color in this figure legend, the reader is referred to the web version of this article.)

important and which deflects vertical motions in meridional direction. Near-inertial currents that are circularly polarized switch from the direction of gravity $\mathbf{g}$ in well-stratified waters to $\mathbf{\Omega}$ in near-homogeneous waters. At mid-latitudes in the latter case, they are observed as strongly elliptically polarized because of the projection of an obliquely tilted circle on a horizontal plane (van Haren and Millot, 2004). In standard Cartesian coordinates (east, north, up(-gravity)), this convection of ultimately neutral stability in the direction of $\mathbf{\Omega}$ implies apparent weak stratification in the direction of $\mathbf{g}$ with, at mid-latitudes, particular preferred 'minimum N-values $N_{\min}$' in terms of a marginally stable gradient Richardson number, expressing the ratio of stabilizing stratification over destabilizing shear (van Haren, 2008). These $N_{\min}$ depend on the type of (non) linear stability. They are estimated as factors of f_h: $N_{\min} = f_h$, $2f_h$ or $4f_h$, for nonlinear, linear and nonlinear stability, respectively.

In this paper, we investigate in detailed observations the character and variability of wave-induced turbulent mixing and restratification in such weakly stratified waters potentially subject to slantwise convection. The observations are made using high-resolution temperature sensors moored in the central-north Alboran Sea, West-Mediterranean (Fig. 1). The immediate (5–10 km horizontal distance) site-surrounding topography is featureless and flat (<0.5% bottom-slope), so that a priori the turbulence character is expected to be different from that above sloping topography where vigorous internal wave breaking in nonlinear bores occurs (e.g., van Haren and Gostiaux, 2012). About 6–25 km southwest of the site, a sub-surface sill forms the nearest potential internal wave generation area near its foot and top, respectively.

Although the Strait of Gibraltar is only about 200 km away with its strong tidal currents and solitary wave generation, those internal waves are not observed in the present area (Watson and Robinson, 1990). Also, the inflow of Atlantic water near the surface is topographically steered southward by the relatively shallow sills around 4°W southwest of the central-north Alboran Sea before turning northeastward again southeast of the central-north Alboran Sea (Fig. 1; e.g., L'Helguen et al., 2002; Skliris and Beckers, 2009; Navarro et al., 2011). Thus, the present mooring site is little affected by Atlantic Ocean influences, except for the barotropic tide, and it is mainly immersed in Mediterranean waters.

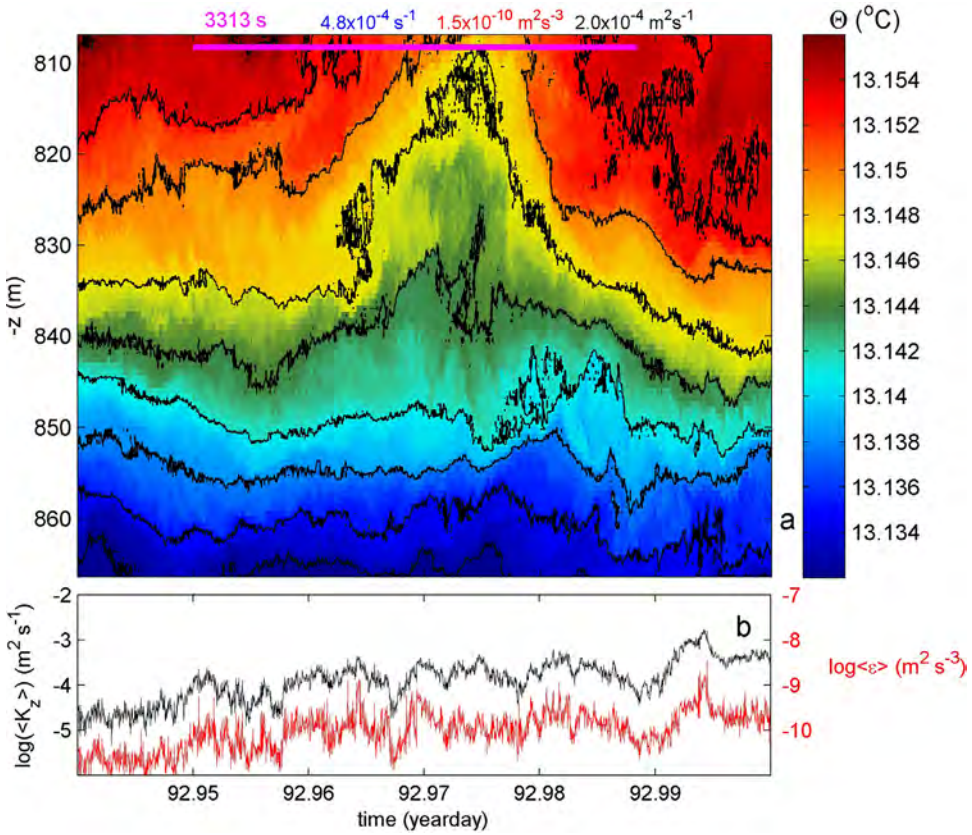

Fig. 5. As Fig. 4, but for a 1.5 h period with a sudden upward motion associated with a high-frequency singular internal quasi-'rogue' wave. Note the different color scale in (a) in comparison with Fig. 4a, for display purposes. Please refer to the overview in Fig. 2 for respective color variations. (For interpretation of the references to color in this figure legend, the reader is referred to the web version of this article.)

2. Materials and methods

2.1. Site and instrumentation

A taut-wire mooring was deployed at $\varphi = 36°24'$N, $\lambda = 3°30'$W, $H = 912$ m water depth between 2 and 11 April, 2013. At this latitude, the local vertical Coriolis parameter, i.e., the inertial frequency, amounts $f = 2\,\Omega \sin \varphi = 0.865 \times 10^{-4}\,\mathrm{s}^{-1}$, whereas $f_h = 1.174 \times 10^{-4}\,\mathrm{s}^{-1}$. The site is more or less the deepest part of the central-north Alboran Sea.

A single elliptic floatation provided 3000 N of net buoyancy at about 107 m from the bottom. With currents of typically less than 0.15 m s^{-1}, the buoy did not move more than 0.1 m vertically and 1 m horizontally, as was verified using pressure and tilt sensors. The float held an upward-looking 75 kHz, four-beam Teledyne-RDI Longranger Acoustic Doppler Current Profiler (ADCP) that sampled at a rate of once per minute. Its deepest good-data level was at 145 m above the bottom (mab), about 40 m above the highest temperature sensor. This was because the ADCP served a different purpose, monitoring currents acoustically over the largest possible range of the (central) water column for a 700 m long test-mooring (not discussed here).

We taped 144 custom-made 'NIOZ4' temperature sensors to the cable at 0.7 m intervals. The sensors sampled at a rate of 1 Hz and were synchronized via induction every 4 h, so that their timing mismatch was <0.02 s. See Appendix A for details on calibrations and the use of these moored temperature data for estimating turbulence parameter values.

Every other day, a shipborne conductivity–temperature–depth (CTD) profile was made for monitoring temperature-salinity variability from 5 m below the surface to 10 m above the bottom, at a horizontal distance of about 1 km from the mooring. A calibrated SeaBird 911plus CTD was used.

In the following, averaging over time is denoted by [. . .], averaging over depth-range by $< \ldots >$. The specific averaging periods and ranges are indicated with the mean values.

2.2. Turbulence estimates using moored thermistors and microstructure profilers

Turbulence parameter estimates using moored high-resolution temperature sensor observations are quite different from those using shipborne or free-falling/rising microstructure profiler observations. The former have high resolution O(1 s) in

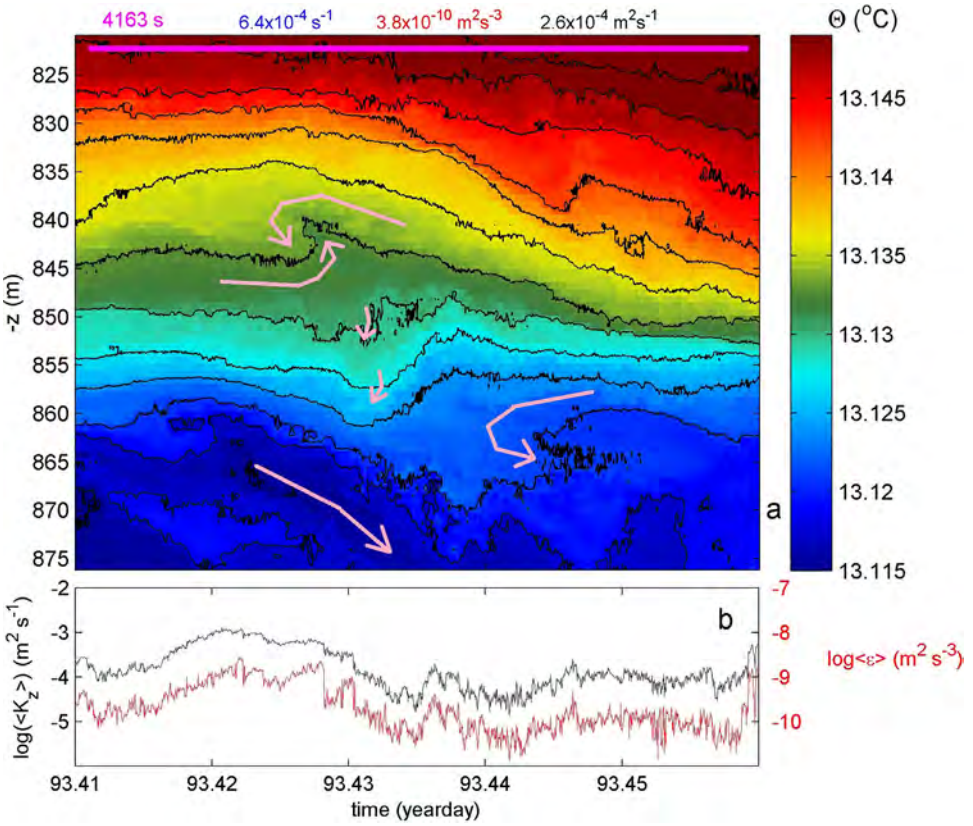

Fig. 6. As Fig. 4, but for a 1.2 h period with a double (oppositely sheared) Kelvin–Helmholtz instability 'KHI'. Note the different color scale in (a). (For interpretation of the references to color in this figure legend, the reader is referred to the web version of this article.)

time, relatively poor resolution O(1 m) in space over a range O(100 m) vertically that is sampled within 0.02 s. It uses the method of density profile reordering for computing the estimates (Thorpe, 1977; Appendix A). Microstructure profilers have a low resolution in time, repeated profiling at a speed of 0.5–0.7 m s^{-1} takes minutes to traverse 100 m and not exactly at the same position due to drift, and high resolution O(10^{-3} m) in vertical space. They use the method of shear (current gradient) and temperature gradient for computing turbulence estimates.

During the present sea campaign no high-resolution microstructure profiler was available. In the past, comparison of turbulence parameter estimates using moored temperature sensors and nearby microstructure profiling resulted in an average agreement to within a factor of two (van Haren and Gostiaux, 2012). This comparison could only be performed for large-scale averages in depth and time, as a compromise between the two methods.

Furthermore, the method of density profile reordering requires averaging over the scale of entire overturns which are O (10 m), generally. As overturns exist inside others, a practical definition of overturn borders is impossible. As a result, a fixed vertical averaging scale of the entire 100 m range of temperature sensors is used here that includes all overturn sizes. Thus, with one exception as an example, only full-range averages of turbulence dissipation rate and diffusivity are meaningful and will be presented in the following. These average values retain the high, 1 s, temporal resolution.

3. Observations

The ~900 m deep, flat-bottom central-north Alboran Sea is dominated by tidal variations and relatively weak stratification (Figs. 2 and 3). In the range between 5 and 105 mab, isotherms seem to vary with the semidiurnal tide for the duration of a few days (e.g., between days 93 and 95). However, variations with time-scales shorter and longer than tidal also occur. They have amplitudes of typically 10–20 m, and occasionally up to 100 m (Fig. 2a). Horizontal currents, measured above the temperature sensor range, vary predominantly with the semidiurnal tide (Fig. 2b), which is due to the proximity of Gibraltar and, thus, the Atlantic Ocean (Fig. 1). Most of the tidal current flows east–west (near-rectilinear current ellipse with $|u| >> |v|$, Fig. 2b) with a local maximum amplitude of 0.03–0.06 m s^{-1}, at 145 mab. Currents are near-homogeneous over the 600 m ADCP range, and shear is low. In addition, a sub-inertial current flows to the ESE, having a magnitude of 0.03 m s^{-1}. In contrast, the vertical current component shows a more erratic time-series behavior, with dominant higher-frequency noise superposed on low-frequency (~inertial) variations. The w have typical amplitudes of 0.005 m s^{-1} (in Fig. 2b, w is multiplied by 10).

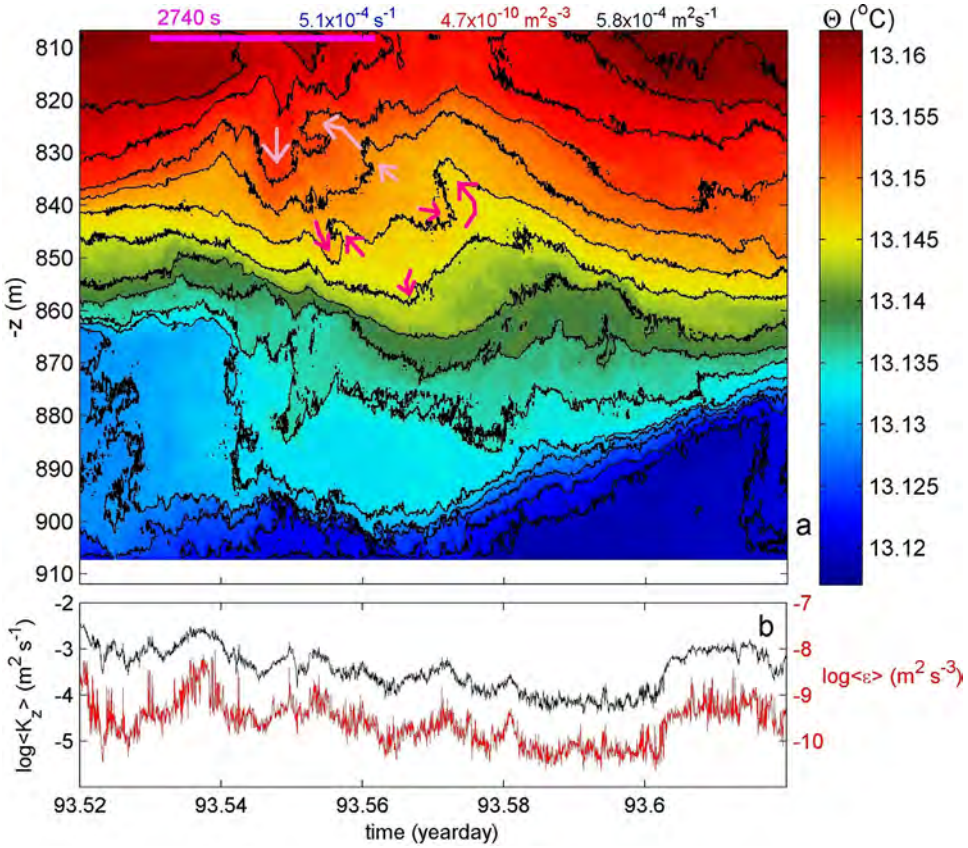

Fig. 7. As Fig. 4, but for a 2.4 h period with a sudden upward motion associated with a double KHI and a large non-linear wave in the lower half. Note the different color scale in (a). (For interpretation of the references to color in this figure legend, the reader is referred to the web version of this article.)

All time-series show a large-scale trend-jump just before day 96. After that day, the isotherm-variations are no longer semidiurnal tide-dominated, in contrast with the u-current component. Then, the sub-inertial v-current becomes stronger southward, whereas the four-day mean vertical current changes from -5×10^{-4} to -1.1×10^{-3} m s^{-1}, a doubling of the tidally averaged downward flow. This trend-jump also shows in the "near"-bottom stratification, of which a much larger range is non-homogeneous over longer periods in the second half of the 9-day record. The occasionally apparent temperature inversions are partially genuine convective instabilities, and partially due to the effects of sensor-drift not accounted for in the 9-day calibration (see Appendix A for the temperature sensor data-processing procedure). In spite of the proximity of Atlantic waters clashing with saltier and warmer Mediterranean waters, the present region is little affected by salinity-compensated intrusions (cf., Fig. A2): the observations were basically made in full-Mediterranean high-salinity waters.

The lower half of the water column is weakly stratified (Figs. 2a and 3a), with a 50 m vertically averaged buoyancy frequency of $N_{50}=5\pm2\times10^{-4\,-1}\approx5\pm2f\approx4\pm1.5f_h$ (Fig. 3a). As a result, the inertio-gravity wave band between frequencies $0.97f<\sigma<1.03$ N is less than a decade wide (LeBlond and Mysak, 1978). Fig. 3a—purple bar demonstrates that the 100 m-range-buoyancy frequency estimated using the moored temperature sensor data and a fixed density–temperature linear relationship compares well, to within 10%, with that from the CTD-observations.

The internal wave bounds are also visible in some 9-day mean frequency spectra (Fig. 3b and c). The w-spectrum jumps half an order of magnitude at $\sigma=4f_h$ (Fig. 3b). At $\sigma<4f_h$, the most elevated part of this spectrum is fairly flat and extends into sub-inertial frequencies, which is typical for w-spectra under weakly stratified conditions (e.g., van Haren and Millot, 2005). It is noted that the (horizontal) kinetic energy 'KE' spectrum peaks at semidiurnal (dominant) and inertial frequencies, but also at $\sigma=2f_h$, before dropping into white noise (having zero-slope). The $2f_h$-sub-peak does not represent a known driving force, but may result from wave–wave interactions. Compared with KE, the temperature spectra are fairly continuous, crossing the internal wave band, from $\sigma<<f$ to $\sigma\approx0.1$ s^{-1} ($\sim10^4$ cpd, cycle per day), which is close to the Nyquist frequency of 4.3×10^4 cpd (half the sampling frequency). This continuation of slope to such high frequencies demonstrates the low noise level of the sensors (cf., Appendix A); between $\sigma=10^3$ and 10^4 cpd the slope is close to $\sigma^{-5/3}$, indicating an inertial sub-range turbulence character, at all depths.

For $\sigma<5\times10^2$ cpd, different temperature spectra and spectral slopes are observed through the range (Fig. 3c). At the two upper levels, green and purple, displayed, a more or less continuous spectrum is found passing the internal wave band to

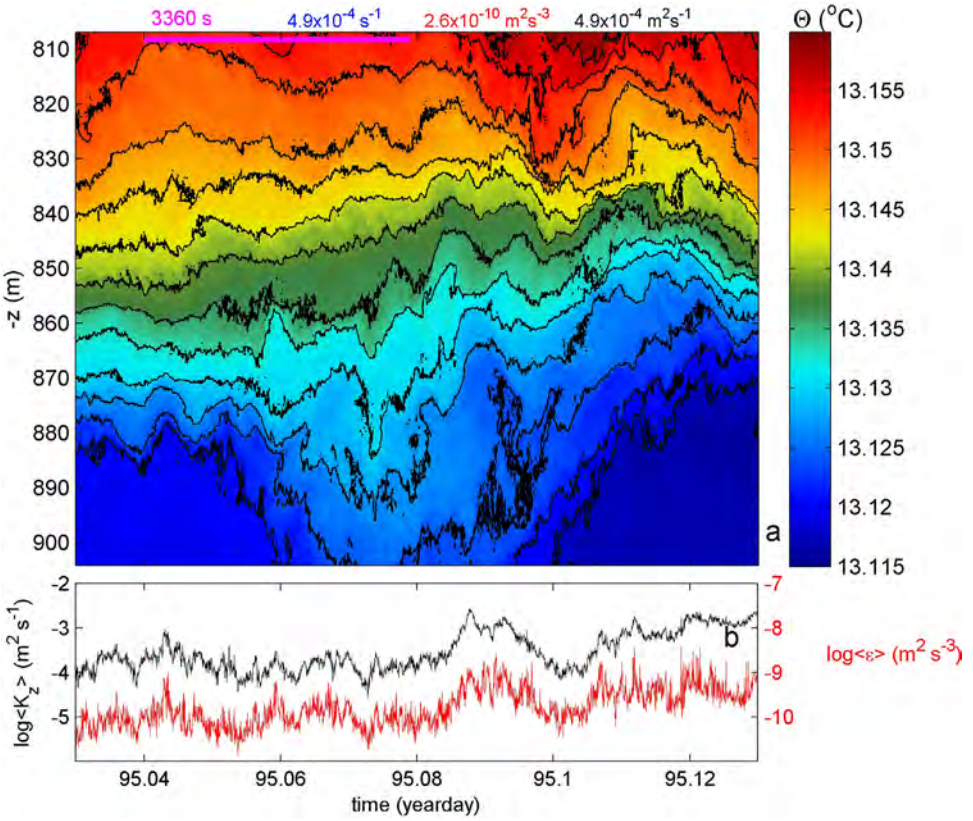

Fig. 8. As Fig. 4, but for a 2.4 h period with a sudden downward motion associated with a high-frequency internal wave penetrating in a weakly stratified near-bottom layer. Note the different color scale in (a). (For interpretation of the references to color in this figure legend, the reader is referred to the web version of this article.)

sub-inertial frequencies. For these spectra, the slope is approximately σ^{-2}, representing the canonical internal wave (Garrett and Munk, 1972) or finestructure (Phillips, 1971) spectral slope. This is found best for the highest level (purple), whereas the green level only clearly does so for $\sigma < 4f_h$ (for which both spectra show approximately the same variance), with lesser slopes in between. Near the bottom (red level) the internal wave band variance is one order of magnitude smaller than that of the higher levels and a clear jump is found at $\sigma = 4f_h$, with a $\sigma^{-5/3}$ slope for lower frequencies and a σ^{-1} slope for higher frequencies to reach the level of turbulence spectrum at about $\sigma = 5 \times 10^2$ cpd. The one-order-of-magnitude jump at $\sigma = 4f_h$ corresponds with the one found for w in Fig. 3b, whereby it is noted that T and w are observed at levels about 140 m apart. Apparently, the internal wave band is defined by $\sim f < \sigma < 4f_h$ throughout the lower half of the water column, while the turbulence regime varies in its redistribution of variance across the frequencies.

3.1. Details of internal waves and turbulence

The transition between turbulence and internal waves is studied in detailed time-depth series of temperature (upper panel of Figs. 4–11). In each of the figures, the time–depth range and the temperature range (color scale) may be different; for reference see Fig. 2a. The particular value of the time–depth-minimum buoyancy period $T_{N\max}$ is given in purple on top besides the time–depth-mean values of buoyancy frequency [$<N>$] (blue), turbulence dissipation rate [$<\varepsilon>$] (red) and turbulent diffusivity [$<K_z>$] (black). Time series of the vertically averaged $<\varepsilon>$ and $<K_z>$ are given in the lowest panel of Figs. 4–11. In Fig. 9, an extra panel is added with all the individual dissipation rate estimates demonstrating large and small overturns, as an example.

A typical half-day of observations (Fig. 4) shows a distinction between the upper and lower halves of the range, with a separation on average at 850 m here. The upper half is more or less continuously weakly stratified, with isotherms oscillating not only slower but also faster than the shortest buoyancy period; see the purple bar for reference. The slower oscillations may be designated as freely propagating internal waves, but the faster ones certainly not. Enhanced stratification is found in thin layers, although seldom of thickness of ~1 m, more commonly larger: O(10 m). In the near-homogeneous layers in between, overturns are observed, some of which are coupled to shear-induced Kelvin–Helmholtz instabilities 'KHI' (e.g., day 92.05, around 850 m). When a particular isotherm is followed, it is found to be smooth most of

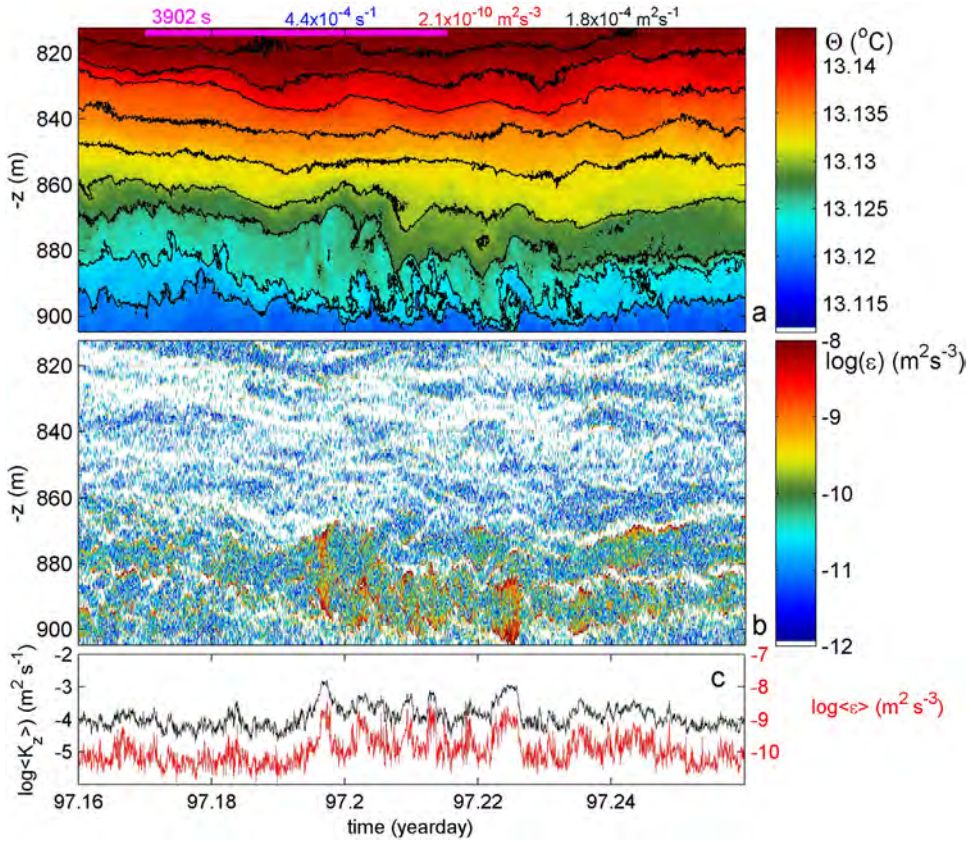

Fig. 9. As Fig. 4, but for a 2.4 h period with rapid (∼350 s duration) overturns in a layer about 25 mab and underneath relatively quiescent 'quasi-internal wave oscillations' that have periods shorter than the smallest buoyancy period. Note the different color scale in (a). Extra panel b shows all individual turbulence dissipation rate estimates. Note that this example can only be used for graphical display, as turbulence quantification should be made over the full individual overturns, as in Thorpe (1977). Here, overturn heights are up to 20 m in the lower layer mainly. Depth–time mean values differ by more than an order of magnitude between the upper and the lower layers. These values are, shallower than 858 m: $[<\varepsilon>] = 1.4 \pm 0.7 \times 10^{-11}\,\mathrm{m^2\,s^{-3}}$, $[<K_z>] = 1.8 \pm 1 \times 10^{-5}\,\mathrm{m^2\,s^{-1}}$ (while $[<N>] = 4.5 \pm 2 \times 10^{-4}\,\mathrm{s^{-1}}$), and below 858 m: $[<\varepsilon>] = 4 \pm 2 \times 10^{-10}\,\mathrm{m^2\,s^{-3}}$, $[<K_z>] = 3.4 \pm 1.6 \times 10^{-4}\,\mathrm{m^2\,s^{-1}}$ (while $[<N>] = 4.3 \pm 2 \times 10^{-4}\,\mathrm{s^{-1}}$). (For interpretation of the references to color in this figure legend, the reader is referred to the web version of this article.)

the time, but it can turn 'rugged' over short periods that do not exceed the minimum buoyancy period: evidence of local turbulent overturning.

The lower half of the range is so weakly stratified that it is regularly found near-homogeneous including statically unstable patches (e.g., around day 92.2, 870 m). In the case that the duration of such unstable patches exceeds the mean local buoyancy period (∼inverse of black value), they are suspect of the effects of salinity-compensated intrusions. That is unlikely so in the present data-set, see also CTD-data in Appendix A. The near-homogeneous character of the lower half is associated with rugged-irregular variations in isotherms, reflecting active turbulent convection. Judging from the isotherm-excursions, the convection 'cells' have vertical scales of some 10 m, in this case. In spite of the (very) weak stratification, turbulence values are still considerable, exceeding open-ocean interior values (e.g., Gregg, 1989; Polzin et al., 1997) by a factor of about 5–10, while being a factor of 100 smaller than above large underwater topography (e.g., Polzin et al., 1997) specifically in intense internal wave breaking areas (van Haren and Gostiaux, 2012).

The variations of the vertically averaged turbulence parameter values around their time-mean, all of duration $t < T_{N\max}$, have a magnitude-range of about two orders of magnitude (Fig. 4b). This range is two orders of magnitude less than in actively internal wave breaking areas. This is probably because the present observations are close to the detection limit (Appendix A). In the example of Fig. 4, the turbulence is observed to vary even less when dominated by the single large convective patch, around day 92.2. In the following, some examples are given of particular internal wave turbulence.

Occasionally, the upper half of the temperature sensor range shows a singular wave intrusion, or upward moving turbulent core when the stratification is rather weak in this part of the range, $N \sim 4f_h$ (Fig. 5). This results in elevated turbulence values but still lower than those for the lower half of the range. The upward moving core or turbulent surge has the appearance of a singular wave. It is not associated with a reversal of horizontal advective (tidal) current.

A similar turbulence level is found around and mainly below a double-shear-induced KHI (Fig. 6). Although the isotherms look considerably less 'thick' or rugged than in Fig. 5, the larger-scale overturns here provide equivalent turbulence,

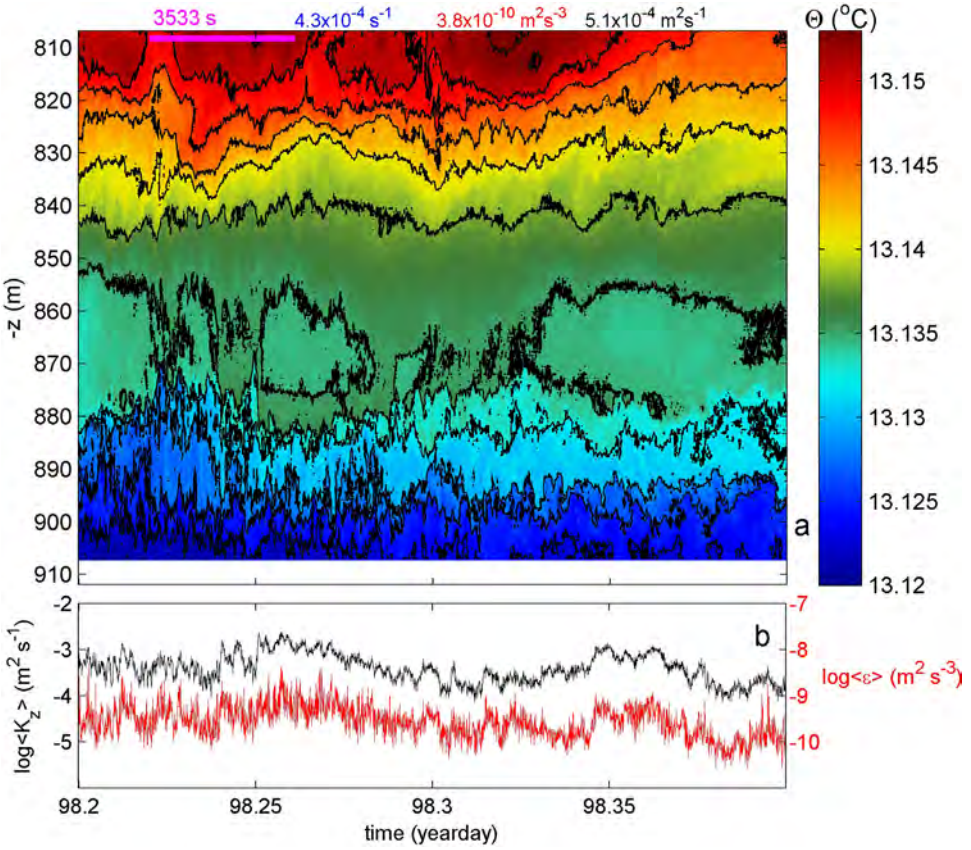

Fig. 10. As Fig. 4, but for a 4.8 h period with vigorous and rapid temperature variations in the weakly stratified layer near the bottom and below a large, near-homogeneous/weak-inversion layer. Note the different color scale in (a). (For interpretation of the references to color in this figure legend, the reader is referred to the web version of this article.)

especially slantwise-convectively in the near-homogeneous part of the range between days 93.42 and 93.43. The less short-scale turbulence is also visible in the vertically averaged values (compare Fig. 6b with Fig. 5b).

The two previous examples can be found combined in a single event of a double KHI forming short-scale upward motions above a large turbulent and near-homogeneous layer (Fig. 7). Here, the near-homogeneous layer does not reach the bottom-end of the temperature sensor range, but a large ∼2 h period nonlinear internal wave pushes a stratified layer up and down across it. Turbulence-patch-periods typically last $\sim 1000\,\mathrm{s} << T_{N\max}$.

Besides upward surges as in Fig. 7 and, especially, Fig. 5, sudden downward motions can occur associated with a high-frequency internal wave penetrating the near-homogeneous 'bottom boundary layer' (Fig. 8; days 95.06–95.08). The currents (at 145 mab; Fig. 2b) do not show evidence as to why the downward motion would occur; it is certainly not associated with a reversal of a (barotropic) tidal current. Most likely, it reflects a high-frequency singular internal wave, having a 'period' of about 2 h, which is between $T_{N\max}$ and $T_{<N>}$ By pushing stratification toward the bottom, turbulence is suppressed. Less than 15 min later (day 95.09), this suppression is followed by enhanced turbulent convection. This and all other, irregular, motions visible in Fig. 8a have periodicities $<T_{N\max}$ and are thus characterized as turbulence.

The apparent internal wave–turbulence motion separation is perhaps most clearly visible during a relatively calm period (Fig. 9; separation here around 860 m). All visible isotherm motions, except those slower than the scale of the entire window, have time-scales $<T_{N\max}$. They thus qualify as turbulence and not as freely propagating internal waves. However, in the upper half of the range some isotherms, in particular the one around 830 m, show fairly small turbulent variations; see also the white low-values band in the example Fig. 9b with all the individual turbulence dissipation rate estimates. For that upper half, turbulence parameters show low values of $[<\varepsilon>] \approx 10^{-11}\,\mathrm{m^2\,s^{-3}}$ and $[<K_z>] \approx 2 \times 10^{-5}\,\mathrm{m^2\,s^{-1}}$, and which are roughly comparable with open-ocean values (Polzin et al., 1997). In the lower half of the temperature sensor range, turbulence parameter values are about 25 times larger. This range is dominated by a fine train of 20 m high convective overturns. These overturns each last about $350\,\mathrm{s} \approx 0.1\,T_{N\max}$.

Relatively vigorous convective overturning is not only observed below a weakly stratified, weakly turbulent layer, but also in intermediate near-homogeneous, strongly convective layers (Fig. 10). As previously noted (Fig. 4), the duration of the convective patches is always found to be $<T_{[<N>]}$. Nevertheless, in Fig. 10 the convection seems different, as around 870 m

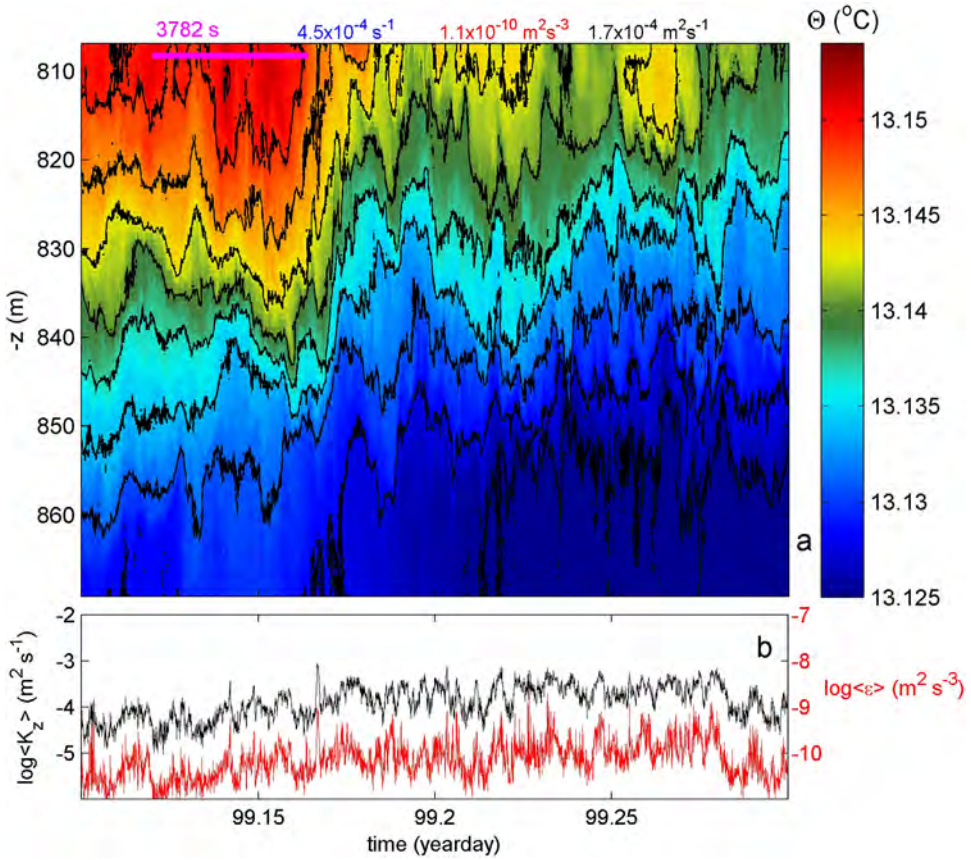

Fig. 11. As Fig. 4, but for a 4.8 h period with a sudden upward motion (∼day 99.17) associated with a high-frequency internal wave. Note the different color scale in (a). (For interpretation of the references to color in this figure legend, the reader is referred to the web version of this article.)

the contours are the most rugged in the image, and around 890 m the motions are rapidly up and down. Apparently, the strongly convective intermediate layer affects the stratification above and below in a partially similar way, as the 840 m-contour does show rapid up/down variations similar to those around 890 m albeit for the first one-third of the image only.

Quasi-regular up and down turbulent motions are also observed higher-up in the range, following a high-frequency nonlinear internal wave frontal passage around day 99.17 (Fig. 11). Behind the front, waves trail having periods of about $1.25\,T_{N\max}$, and which are superseded with much shorter 'quasi-periodic' turbulent motions. Initially up to day 99.16, the isotherms are rather smooth throughout, a result of weak turbulence. After the turbulence peak on day 99.17 however, the isotherms become more rugged especially in the lower half of the range, resulting in an increase of turbulence by a factor of 5, approximately lasting until day 99.28 (Fig. 11b).

4. Concluding remarks

We have studied in some detail a 100-m-vertically varying 'bottom boundary layer' above a flat bottom. Such a large-varying near-homogeneous layer cannot be established via bottom friction of the 0.06 m s^{-1} amplitude tidal currents or the $<$0.1 m s^{-1} amplitude sub-inertial currents (Ekman, 1905; Maas and van Haren, 1987). The 'Ekman dynamics', indicating a balance between frictional and Coriolis forces, predicts a layer-thickness of a few m maximum. This is below the present temperature sensor range. A different mechanism which can drive the observed 1–100 m large convection is related with internal waves combined with the effects of the earth rotation. Although inertial waves are the only internal waves that can always propagate freely between stratified and homogeneous waters (van Haren and Millot, 2005), and as they are dominant in large parts the Mediterranean, it is found that other large-scale internal waves may trigger convection in weakly stratified seas.

Here, the variation in internal wave environment is reflected in the vertical density stratification. Nearby CTD-observations suggest a blocking of weak stratification at $N \approx 4f_h$ (below 550 m), definitely at $2f_h$ (below 700 m). These two specific buoyancy frequencies designate particular stability in stratification, usually in thin layers, that balances shear by neutral stability convective motions in the direction of the earth rotational vector (van Haren, 2008).

As the present observations are 1D(space)-time, it cannot be established whether the down- and upward motions represent a 3D-vortex, suggesting a similarity with [water] sprout emanating from unstable clouds. Thus, the precise dimensions and evolution, also with time, of the convective tubes remain unclear, although they are found to be O(10) m in the vertical and occasionally >100 m. Further specification awaits proper 3D mooring efforts, with horizontal scales similar to the vertical ones employed here.

Acknowledgments

I thank captain and crew of the R/V Pelagia and NIOZ-MTM for deployment and recovery of the instrumentation. I thank M. Laan and L. Gostiaux for their ceaseless thermistor efforts. This work has been funded in part by the Netherlands Organization for Scientific Research (NWO).

Appendix A.

Calibrating temperature sensor data to density variations

High-resolution temperature sensors have the potential to quantify vertical turbulent exchange across density-stratified waters, when a number of conditions are satisfied. Depending on the rate of stratification and the amount of turbulence energy input, the relevant vertical scales need to be resolved by adequate sensor spacing and numbers. For open-ocean and deep-sea internal-wave-breaking-turbulence above sloping topography, scales O(1) and O(100) m, respectively, seem adequate. Under weakly stratified conditions, careful calibration is needed to resolve temperature well below the 0.001 °C (1 mK) level, not necessarily in absolute accuracy but in relative precision. Finally, temperature is to be translated to density variations, preferably to the same precision as temperature and with a known contribution of salinity without inversions.

The NIOZ4 temperature sensor noise level is $<6\times10^{-5}$ °C (van Haren et al., 2009; NIOZ4 is an update of NIOZ3 with similar characteristics) and thus potentially of sufficient precision. Previous in situ calibration against SeaBird SBE-911plus CTD, via the mounting of crates of sensors or a cable with attached sensors in the CTD-Rosette frame and lowering the package in near-homogeneous ocean-layers, provided calibration-accuracies of about 0.001 °C. Recently, NIOZ-technicians constructed a laboratory calibration-tank with the capacity of 200 sensors that are calibrated against an SBE35 Deep Ocean Standards high precision platinum thermometer to an accuracy of 2×10^{-4} °C for ranges of about 15 °C (unpublished results). Due to drift in the NTC and other electronics of the sensors, such accuracy can be maintained for a period of about 1–2 weeks, which is generally shorter than the mooring period (of up to 1.5 years). In post-processing, sensor-drifts are corrected by subtracting constant deviations from a smooth profile over the entire vertical range and averaged over typical periods of 4–7 days (unpublished results). In weakly stratified waters as the present observations, the remaining deviations then approach the standard noise level of about 5×10^{-5} °C (Fig. A1).

The calibrated temperature sensor data are transferred to conservative (∼potential) temperature (θ) values (McDougall et al., 2009), before they are used as a tracer for potential density variations $\delta\sigma_{1000}$, referenced to 1000 m, following a constant linear relationship obtained from best-fit data using all nearby CTD-profiles over the mooring period and across the lower 200 mab, twice the range of the temperature sensors (Fig. A2). As the CTD-temperature is considerably less noisy than salinity and density (which are computed using combined temperature and conductivity data), compare Fig. A2a with b and c which have the same x-axis range in terms of density, some compromise is necessarily made in using this relationship's slope $\alpha=\delta\sigma_{1000}/\delta\theta=-0.066\pm0.002$ kg m^{-3} °C^{-1} ($n=5$). It is stressed that hereby the low-noise level of the temperature sensors is used to its full capacity, but only under the strict condition of this relationship. However, salinity and temperature may behave differently in other parts of seas and oceans. Their relationship should always be verified, for example using CTD. The number of moored temperature sensors here (144) and the 0.7 m-resolution are potentially sufficient to estimate turbulence parameters from the weakly stratified Mediterranean waters. This is because these estimates are not made via resolution of the smallest Kolmogorov-scales O(10^{-3} to 10^{-2}) m of turbulence dissipation, but through the resolution of scales of up to the largest energy-containing Ozmidov-scales O(10 m) of turbulence in stratified seas.

Thereby, turbulent kinetic energy dissipation rate $\varepsilon=0.64\,d^2N^3$ and vertical (z) turbulent eddy diffusivity $K_z=0.128\,d^2N$ are estimated by calculating 'overturning' scales d after reordering every 1 Hz time-step the potential density (temperature) profile, which may contain inversions, into a stable monotonic profile without inversions (Thorpe, 1977, 1987). Here, $N=(-g/\rho_0\delta\sigma_{1000}/\delta z)^{1/2}$, with g denoting the acceleration of gravity and $\rho_0=1027$ kg m^{-3} a reference density, is computed from the reordered statically stable profile. The value of 0.64 follows from a comparison between overturning and Ozmidov scales by Dillon (1982), which showed considerable variation over one order of magnitude with time and depth (see also, Wesson and Gregg, 1994; Carniel et al., 2012). In K_z, a constant mixing efficiency of 0.2 is used, which is common under turbulent oceanographic conditions (Osborn, 1980; Dillon, 1982; Oakey, 1982; Stansfield et al., 2001) although debate is ongoing as it may be variable under conditions like salt fingering and in particular layers in the interior (e.g., St. Laurent and Schmitt, 1999). As the noise level of the temperature sensors is very low (Fig. A1b), the threshold for detecting overturns is mainly due to remaining temperature-shifts after calibration ($<5\times10^{-4}$ °C; van Haren et al., 2009; van Haren and Gostiaux, 2012). The resolvable turbulence dissipation rate threshold averaged over the entire 100 m vertical range is approximately 3×10^{-12} m^2 s^{-3}.

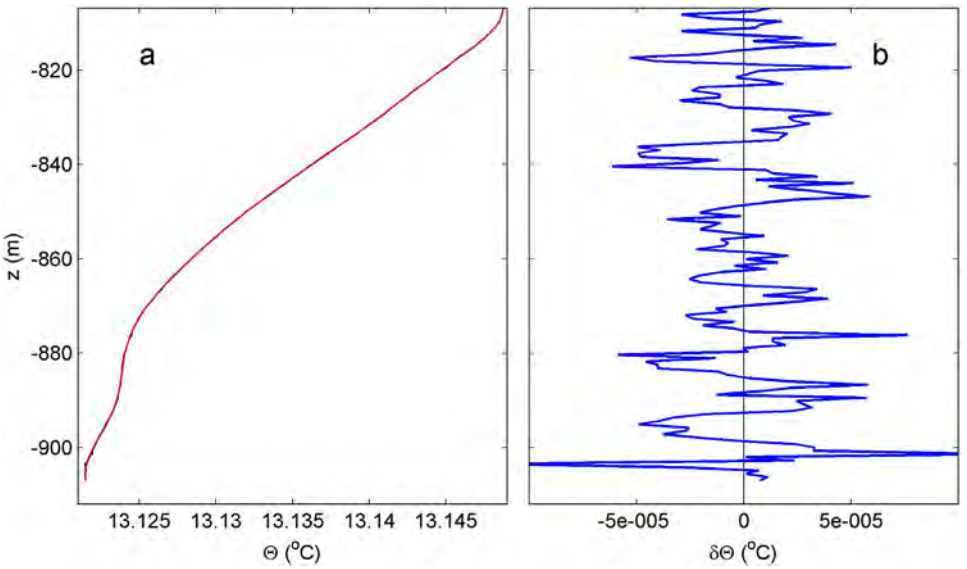

Fig. A1. Four-day mean moored sensor data (every 500th profile taken) after being fit to their calibration polynomial. (a) Conservative temperature. Data are in black and barely visible; high-order polynomial fit is in red. (b) Difference between the two profiles in (a). (For interpretation of the references to color in this figure legend, the reader is referred to the web version of this article.)

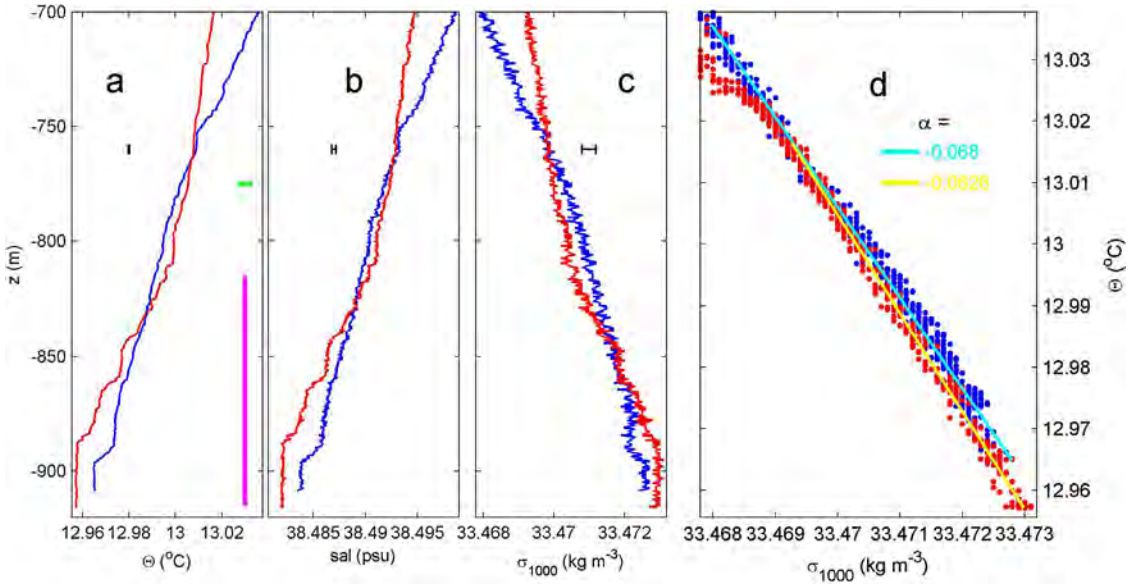

Fig. A2. Lower 200 m of two (of five) CTD-profiles near the mooring. Blue data are from around the beginning of the moored period, red from near the end. (a) Conservative temperature. The vertical purple bar indicates the range of the moored temperature sensors. The horizontal green bar indicates the (10 m-average) depth of the current data in Fig. 2b. The small black line indicates the tiny instrumental noise level, of the size of the line thickness. (b) Salinity with x-axis range matching the one in (a). in terms of equivalent relative contributions to density variations. The noise level is considerably larger than for temperature. (c) Density anomaly referenced to 1000 m. Due to salinity contributions, the noise level error bar is larger than for temperature. (d) Density anomaly–conservative temperature relationship ($\delta\sigma_{1000} = \alpha\delta\Theta$). The data yielding the two extreme slopes are indicated (the mean of 5 profiles gives $<\alpha> = -0.066 \pm 0.002$ kg $m^{-3} {}^{\circ}C^{-1}$). (For interpretation of the references to color in this figure legend, the reader is referred to the web version of this article.)

References

Carniel, S., Kantha, L.H., Book, J.W., Sclavo, M., Prandke, H., 2012. Turbulence variability in the upper layers of the southern Adriatic Sea under a variety of atmospheric forcing conditions. Cont. Shelf Res. 44, 39–56.
Dillon, T.M., 1982. Vertical overturns: a comparison of Thorpe and Ozmidov length scales. J. Geophys. Res. 85, 9601–9613.

Ekman, V.W., 1905. On the influence of the earth's rotation on ocean currents. Ark. Mat. Astron. Fys. 2, 1–52.
Garrett, C.J.R., Munk, W.H., 1972. Space-time scale of internal waves. Geophys. Fluid Dyn. 3, 225–264.
Gregg, M.C., 1989. Scaling turbulent dissipation in the thermocline. J. Geophys. Res. 94, 9686–9698.
Gerkema, T., Zimmerman, J.T.F., Maas, L.R.M., van Haren, H., 2008. Geophysical and astrophysical fluid dynamics beyond the traditional approximation. Rev. Geophys. 46, RG2004. doi:http://dx.doi.org/10.1029/2006RG000220.
LeBlond, P.H., Mysak, L.A., 1978. Waves in the Ocean. Elsevier, Amsterdam NL, pp. 602.
L'Helguen, S., Le Corre, P., Madec, C., Morin, P., 2002. New and regenerated production in the Almeria–Oran front area, eastern Alboran Sea. Deep-Sea Res. I 49, 83–99.
Maas, L.R.M., van Haren, J.J.M., 1987. Observations on the vertical structure of tidal and inertial currents in the central North Sea. J. Mar. Res. 45, 293–318.
Marshall, J., Schott, F., 1999. Open-ocean convection: observations theory, and models. Rev. Geophys. 45, 1–64.
McDougall, T.J., Feistel, R., Millero, F.J., Jackett, D.R., Wright, D.G., King, B.A., Marion, G.M., Chen, C.-T.A., Spitzer, P., 2009. Calculation of the thermodynamic properties of seawater, Global ship-based repeat hydrography manual. IOCCP Report 14, ICPO Publication Series 134, (U.N.E.S.C.O., Paris, F).
Navarro, G., Vazquez, A., Macias, D., Bruno, M., Ruiz, J., 2011. Understanding the patterns of biological response to physical forcing in the Alboran Sea (western Mediterranean). J. Geophys. Res. 38, L23606. doi:http://dx.doi.org/10.1029/2011GL049708.
Oakey, N.S., 1982. Determination of the rate of dissipation of turbulent energy from simultaneous temperature and velocity shear microstructure measurements. J. Phys. Oceanogr. 12, 256–271.
Osborn, T.R., 1980. Estimates of the local rate of vertical diffusion from dissipation measurements. J. Phys. Oceanogr. 10, 83–89.
Phillips, O.M., 1971. On spectra measured in an undulating layered medium. J. Phys. Oceanogr. 1, 1–6.
Polzin, K.L., Toole, J.M., Ledwell, J.R., Schmitt, R.W., 1997. Spatial variability of turbulent mixing in the abyssal ocean. Science 276, 93–96.
Sheremet, V.A., 2004. Laboratory experiments with tilted convective plumes on a centrifuge: a finite angle between the buoyancy and the axis of rotation. J. Fluid Mech. 506, 217–244.
Skliris, N., Beckers, J.-M., 2009. Modelling the Gibraltar Strait/Western Alboran Sea ecohydrodynamics. Ocean Dyn. 59, 489–508.
Stansfield, K., Garrett, C., Dewey, R., 2001. The probability distribution of the Thorpe displacement within overturns in Juan de Fuca Strait. J. Phys. Oceanogr. 31, 3421–3434.
St. Laurent, L., Schmitt, R.W., 1999. The contribution of salt fingers to vertical mixing in the North Atlantic tracer release experiment. J. Phys. Oceanogr. 29, 1404–1424.
Straneo, F., Kawase, M., Riser, S.C., 2002. Idealized models of slantwise convection in a baroclinic flow. J. Phys. Oceanogr. 32, 558–572.
Thorpe, S.A., 1977. Turbulence and mixing in a Scottish loch. Philos. Trans. R. Soc. Lond. A 286, 125–181.
Thorpe, S.A., 1987. Current and temperature variability on the continental slope. Philos. Trans. R. Soc. Lond. A 323, 471–517.
van Haren, H., 2008. Abrupt transitions between gyroscopic and internal gravity waves: the mid-latitude case. J. Fluid Mech. 598, 67–80.
van Haren, H., Gostiaux, L., 2012. Detailed internal wave mixing above a deep-ocean slope. J. Mar. Res. 70, 173–197.
van Haren, H., Millot, C., 2004. Rectilinear and circular inertial motions in the Western Mediterranean Sea. Deep-Sea Res. I 51, 1441–1455.
van Haren, H., Millot, C., 2005. Gyroscopic waves in the Mediterranean Sea. Geophys. Res. Lett. 32, L24614. doi:http://dx.doi.org/10.1029/2005GL023915.
van Haren, H., Laan, M., Buijsman, D.-J., Gostiaux, L., Smit, M.G., Keijzer, E., 2009. NIOZ3: independent temperature sensors sampling yearlong data at a rate of 1 Hz. IEEE J. Ocean. Eng. 34, 315–322.
Watson, G., Robinson, I.S., 1990. A study of internal wave propagation in the Strait of Gibraltar using shore-based marine radar images. J. Phys. Oceanogr. 20, 374–395.
Wesson, J.C., Gregg, M.C., 1994. Mixing at Camarinal Sill in the Strait of Gibraltar. J. Geophys. Res. 99, 9847–9878.